Ordered Mesoporous Bioactive Glasses for Bone Tissue Regeneration

A. López-Noriega,[†] D. Arcos,*[,†] I. Izquierdo-Barba,[‡,§] Y. Sakamoto,[‡] O. Terasaki,[‡] and M. Vallet-Regí*[,†]

Departamento Química Inorgánica y Bioinorgánica, Facultad de Farmacia, Universidad Complutense de Madrid, 28040 Madrid, Spain, and Stockholm University, Arrhenius Lab, S-10691 Stockholm, Sweden

Received February 28, 2006. Revised Manuscript Received April 28, 2006

A series of ordered mesoporous $SiO_2-CaO-P_2O_5$ sol−gel glasses which are highly bioactive has been synthesized through evaporation-induced self-assembly in the presence of a nonionic triblock copolymer, $EO_{20}PO_{70}EO_{20}$ (P123), template. By keeping constant the $SiO_2 + P_2O_5$/P123 ratio, the influence of the CaO precursor, $Ca(NO_3)_2{\cdot}4H_2O$, on the mesostructure has been determined. After calcination at 700 °C, ordered mesoporous glasses are obtained, showing structures that evolve from 3D-cubic to 2D-hexagonal when the CaO content increases. The mesoporous glasses are highly bioactive compared with conventional ones, due to the increased textural characteristics supplied by the template. The bioactivity tests point out that the surface area, porosity, and 3D-structure become more important than chemical composition during the apatite crystallization stage in these materials, due to the very high textural parameters obtained.

Introduction

Since 1991, when scientists of Mobil Oil Corporation synthesized the silica-based MCM-41 molecular sieve,[1−2] highly ordered mesoporous materials have attracted the attention of many scientists, mainly due to their potential technological applications. Mesoporous materials are characterized as having high surface area, pore volume, and pore size, with narrow pore diameter distribution. For this reason, applications in the field of catalysis, lasers, sensors, solar cells, etc. have been proposed and/or developed.[3−8]

Recently, these materials have been proposed for their application in biomaterials science.[9] Due to their textural properties of surface and porosity, ordered mesoporous materials have shown to be excellent candidates for two biomedical applications: local drug delivery systems[10−12] and bone tissue regeneration.[13−15] Actually, silica-based mesoporous materials are able to incorporate high dosages of drugs into the mesopores. On the other side, mesoporous materials can be synthesized with analogous chemical composition to highly bioactive sol−gel glasses. These materials are able to bond to living bone when implanted through the formation of a nonstoichiometric carbonated hydroxyapatite of nanometrical size (CHA).[16,17] This *bioactive bond* ensures the implant osteo-integration, and its degradation products promote the bone tissue regeneration.

Increasing the specific surface area and pore volume of bioactive glasses greatly accelerates the CHA formation and therefore enhances the bioactive behavior.[18] In this sense, highly ordered mesoporous materials provide very promising possibilities in the field of bone tissue regeneration. Moreover, these materials can be loaded with osteogenic agents promoting the new bone formation in vivo and can also be applied as scaffolds for bone tissue engineering.[19,20]

Nonionic block copolymers are an interesting class of structure-directing agents whose self-assembly characteristics lead to ordered mesostructures.[21−25] They have the advantage that their ordering properties can be tuned by adjusting

* Corresponding authors.
[†] Universidad Complutense de Madrid.
[‡] Stockholm University.
[§] Permanent address: Departamento Química Inorgánica y Bioinorgánica, Facultad de Farmacia, Universidad Complutense de Madrid, 28040 Madrid, Spain.

(1) Kresge, C. T.; Leonowicz, M. E.; Roth, W. J.; Vartulli, J. C.; Beck, J. S. *Nature* **1992**, *359*, 710.
(2) Beck, J. S.; Vartulli, J. C.; Roth, W. J.; Leonowicz, M. E.; Kresge, C. T.; Schmitt, K. D.; Chu, C. T. W.; Olson, D. H.; Sheppard, E. W.; McCullen, S. B.; Higgings, J. B.; Schlenker, J. L. *J. Am. Chem. Soc.* **1992**, *114*, 10834.
(3) Ying, J. Y.; Mehnert, P.; Wong, M. S. *Angew. Chem., Int. Ed.* **1999**, *38*, 56.
(4) Brinker, C. J. *Curr. Opin. Solid State Mater. Sci.* **1996**, *1*, 798.
(5) Sayari, A. *Chem. Mater.* **1996**, *8*, 1840.
(6) Yang, H.; Kuperman, A.; Coombs, N.; Mamiche-Afara, S.; Ozin, G. A. *Nature* **1996**, *379*, 703.
(7) Davis, M. E. *Nature* **2002**, *417*, 813.
(8) Stein, A. *Adv. Mater.* **2003**, *15*, 763.
(9) Vallet-Regí, M.; Ruiz-González, L.; Izquierdo-Barba, I. González-Calbet, J. M. *J. Mater. Chem.* **2006**, *16*, 26.
(10) Salonen, J.; Laitinen, L.; Kaukonen, A. M.; Tuura, J.; Bjorkqvist, M.; Heikkila, T.; Vaha-Heikkila, K.; Hirvonen, J.; Lehto, V. P. *J. Controlled Release* **2005**, *108*, 362.
(11) Izquierdo-Barba, I.; Martinez, A.; Doadrio, A. L.; Perez-Pariente, J.; Vallet-Regi, M. *Eur. J. Pharm. Sci.* **2005**, *26*, 365.
(12) Yang, Q.; Wang, S. H.; Fan, P. W.; Wang, L. F.; Di, Y.; Lin, K. F.; Xiao, F. S. *Chem. Mater.* **2005**, *17*, 5999.
(13) Vallet-Regi, M.; Izquierdo-Barba, I.; Ramila, A.; Perez-Pariente, J.; Babonneau, F.; Gonzalez-Calbet, J. M. *Solid State Sci.* **2005**, *7*, 233.
(14) Yan, X. X.; Yu, C. Z.; Zhou, X. F.; Tang, J. W.; Zhao, D. Y. *Angew. Chem., Int. Ed.* **2004**, *43*, 5980.
(15) Yan, X. X.; Deng, H. X.; Huang, X. H.; Lu, G. Q.; Qiao, S. Z.; Zhao, D. Y.; Yu, C. Z. *J. Non-Cryst. Solids* **2005**, *351*, 3209.
(16) Hench, L. L. *Science* **1980**, *208*, 826.
(17) Vallet-Regí, M. *J. Chem. Soc., Dalton Trans.* **2001**, *2*, 97.
(18) Vallet-Regí, M.; Ragel, C. V.; Salinas, A. J. *Eur. J. Inorg. Chem.* **2003**, *6*, 1029.
(19) Hench, L. L.; Polack, J. M. *Science* **2002**, *295*, 1014.
(20) Langer, R.; Vacanti, J. P. *Science* **1993**, *260*, 920.

10.1021/cm060488o CCC: $33.50
Published on Web 05/28/2006

Table 1. Nominal Composition (mol %) and Amounts of Reactants (g) of the Mesoporous Bioactive Glasses (MBG)[a]

sample code	nominal composition (% mol)	TEOS (g)	TEP (g)	$Ca(NO_3)_2 \cdot 4H_2O$ (g)	H_2O (total amount, g)	surfactant concn (wt %)[b]
S58m	SiO_2 58−CaO 37−P_2O_5 5	3.49	0.51	2.47	1.25	62
S75m	SiO_2 75−CaO 20−P_2O_5 5	3.58	0.42	1.10	0.83	71
S85m	SiO_2 85−CaO 10−P_2O_5 5	3.70	0.34	0.49	0.64	76

[a] All the synthesis were carried out with 2 g of P123, 0.5 mL of 0.5 N HCl, and 30 g of ethanol. [b] The surfactant concentration is calculated with respect to the total amount of water, under the assumption that all the ethanol is previously evaporated.

solvent composition, molecular weight, or copolymer architecture. Depending on the amphiphilic block copolymer used as the structure-directing agent, two-dimensional (2D) hexagonal and three-dimensional (3D) cubic mesoporous structures can be obtained.[26−34] However, the chemical composition of the copolymer is not the only factor that determines the final mesostructure. The material's morphology (monolith, film, membrane, etc.)[35−39] and synthesis conditions, such as temperature, ionic strength, acidity, and reactant ratios, also have an influence on the mesophase ordering.[40−45] All these variables must be taken into account when applying this synthesis route to bioceramics, as the bioactive process is a surface process and the response of the living tissue will be ruled by the surface characteristics of the implant.[46,47]

In this work we have obtained ordered mesoporous materials in the system SiO_2−CaO−P_2O_5, with different CaO contents. By changing the CaO content the bioactive behavior can be modified due to the different network connectivity and the textural properties. This article also shows that the mesostructural ordering can also be tailored by the CaO precursor addition. Finally, a new insight of the factors involved in the bioactivity process is discussed for mesoporous sol−gel glasses, which have much higher textural properties than the conventional ones.

Materials and Methods

Highly ordered mesoporous SiO_2−P_2O_5−CaO sol−gel glasses were synthesized by using a commercially available nonionic surfactant Pluronic P123 (BASF) as the structure-directing agent. P123 is an amphiphilic triblock copolymer having the sequence poly(ethylene oxide)−poly(propylene oxide)−poly(ethylene oxide) (PEO−PPO−PEO), $EO_{20}PO_{70}EO_{20}$ (M_{ave} = 5800). An evaporation-induced self-assembly (EISA)[48] process was applied for the synthesis of bioactive mesoporous glasses. Tetraethyl orthosilicate (TEOS), triethyl phosphate (TEP), and calcium nitrate, $Ca(NO_3)_2 \cdot 4H_2O$, (Aldrich) were used as SiO_2, P_2O_5, and CaO sources, respectively. Three different compositions were synthesized, denoted as S58m, S75m, and S85m. The amount of reactants and final compositions are collected in Table 1. In a typical synthesis 2 g of P123 were dissolved in 30 g of ethanol with 0.5 mL of 0.5 N HCl solution. Afterward TEOS, TEP, and $Ca(NO_3)_2 \cdot 4H_2O$ were added under continuous stirring in 3 h intervals. The sols were cast in Petri dishes (9 cm diameter) to undergo the EISA process at room temperature. The gelation process occurred after 35 h, and the gels were aged for 7 days in the Petri dish at room temperature. Finally, the dried gels were removed as homogeneous and transparent membranes (several hundreds of micrometers thick) and treated at 700 °C for 3 h to obtain the final calcined glass powder.

Powder X-ray diffraction experiments were performed with a Philips X'Pert diffractometer equipped with Cu Kα radiation (wavelength 1.5406 Å). XRD patterns were collected in the 2θ range between 1° and 4° with a step size of 0.02° and counting time of 5 s per step. The textural properties of the calcined materials were determined by nitrogen adsorption porosimetry by using a Micromeritics ASAP 2010. To perform the N_2 adsorption measurements, the samples were previously degassed under vacuum for 24 h, at 120 °C. The surface area was determined using the Brunauer−Emmett−Teller (BET) method. The pore size distribution between 0.5 and 40 nm was determined from the desorption branch of the isotherm by means of the Barret−Joyner−Halenda (BJH) method. Transmission electron microscopy (TEM) was carried out with a JEOL-3010 microscope, operating at 300 kV (Cs 0.6 mm, resolution 1.7 Å). Images were recorded using a CCD camera (model Keen view, SIS analyses size 1024 × 1024, pixel

(21) Zhao, D. Y.; Huo, Q. S.; Feng, J. G.; Chmelka, B. F.; Stucky, G. D. *J. Am. Chem. Soc*. **1998**, *120*, 6024.
(22) Zhao, D. Y.; Feng, J. L.; Huo, Q. S.; Melosh, N.; Fredrickson, G. H.; Chmelka, B. F.; Stucky, G. D. *Science* **1998**, *279*, 548.
(23) Yang, P. D.; Zhao, D. Y.; Margolese, D. I.; Chmelka, B. F.; Stucky, G. D. *Nature* **1998**, *396*, 152.
(24) Yu, C. Z.; Fan, J.; Tian, B. Z.; Stucky, G. D.; Zhao, D. Y. *J. Phys. Chem. B* **2003**, *107*, 13368.
(25) Tian, B. Z.; Liu, X. Y.; Zhang, Z. D.; Tu, B.; Zhao, D. Y. *J. Solid State Chem*. **2002**, *167*, 324.
(26) Chan, Y. T.; Lin, H. P.; Mou, C. Y.; Liu, S. T. *Chem. Commun*. **2002**, 2878.
(27) Melosh, N. A.; Lipic, P.; Bates, F. S.; Wudl, F.; Stucky, G. D.; Fredrickson, G. H.; Chmelka, B. F. *Macromolecules* **1999**, *32*, 4332.
(28) Zhang, Z. D.; Yan, X. X.; Tian, B. Z.; Shen, S. D.; Chen, D. H.; Zhu, G. S.; Qiu, S. L.; Zhao, D. Y. *Chem. Lett.* **2005**, *34*, 182.
(29) Che, S. N.; Garcia-Bennett, A. E.; Liu, X. Y.; Hodgkins, R. P.; Wright, P. A.; Zhao, D. Y.; Terasaki, O.; Tatsumi, T. *Angew. Chem., Int. Ed*. **2003**, *42*, 3930.
(30) Liu, X. Y.; Tian, B. Z.; Yu, C. Z.; Gao, F.; Xie, S. H.; Tu, B.; Che, R. C.; Peng, L. M.; Zhao, D. Y. *Angew. Chem. Int. Ed.* **2002**, *41*, 3876.
(31) Yu, C. Z.; Yu, Y. H.; Zhao, D. Y. *Chem. Commun*. **2000**, 575.
(32) Zhao, D. Y.; Yang, P. D.; Margolese, D. I.; Chmelka, B. F.; Stucky, G. D. *Chem. Commun*. **1998**, 2499.
(33) Flodström, K.; Alfredsson, V. *Microporous Mesoporous Mater*. **2003**, *59*, 167.
(34) Soler-Illia, G. J. D. A.; Crepaldi, E. L.; Grosso, D.; Sanchez, C. *Curr. Opin. Colloid Interface Sci*. **2003**, *8*, 109.
(35) Zhou, X. F.; Yu, C. Z.; Tang, J. W.; Yan, X. X.; Zhao, D. Y. *Microporous Mesoporous Mater*. **2005**, *79*, 283.
(36) Yang, H. F.; Shi, Q. H.; Tian, B. Z.; Xie, S. H.; Zhang, F. Q.; Yan, Y.; Tu, B.; Zhao, D. Y. *Chem. Mater*. **2003**, *15*, 536.
(37) Xu, A. W.; Yu, J. C.; Zhang, H. X.; Zhang, L. Z.; Kuang, D. B.; Fang, Y. P. *Langmuir* **2002**, *18*, 9570.
(38) Zhao, D.; Yang, P.; Melosh, N.; Feng, J.; Chmelka, B. F.; Stucky, G. D. *Adv. Mater*. **1998**, *10*, 1380.
(39) Ogawa, M. *Chem. Commun*. **1996**, 1149.
(40) Pei, L.; Kurumada, K. I.; Tanigaki, M.; Hiro, M.; Susa, K. *J. Mater. Sci*. **2004**, *39*, 4045.
(41) Yu, C. Z.; Fan, J.; Tian, B. Z.; Zhao, D. Y. *Chem. Mater*. **2004**, *16*, 889.
(42) Bao, X. Y.; Zhao, X. S.; Li, X.; Li, J. *Appl. Surf. Sci*. **2004**, *237*, 380.
(43) Bennadja, Y.; Beaunier, P.; Margolese, D.; Davidson, A. *Microporous Mesoporous Mater*. **2001**, *44−45*, 147.
(44) Tang, J. W.; Yu, C. Z.; Zhou, X. F.; Yan, X. X.; Zhao, D. Y. *Chem. Commun*. **2004**, 2240.
(45) Yu, C. Z.; Tian, B. Z.; Fan, B.; Stucky, G. D.; Zhao, D. Y. *Chem. Commun*. **2001**, 2726.
(46) Hench, L. L.; Splinter, R. J.; Greenlee, T. K.; Allen, W. C. *J. Biomed. Mater. Res*. **1971**, *2*, 117.
(47) Vallet-Regí, M.; Arcos, D.; Pérez-Pariente, J. *J. Biomed. Mater. Res*. **2000**, *51*, 23.
(48) Brinker, C. J.; Lu, Y. F.; Sellinger, A.; Fan, H. Y. *Adv. Mater*. **1999**, *11*, 579.

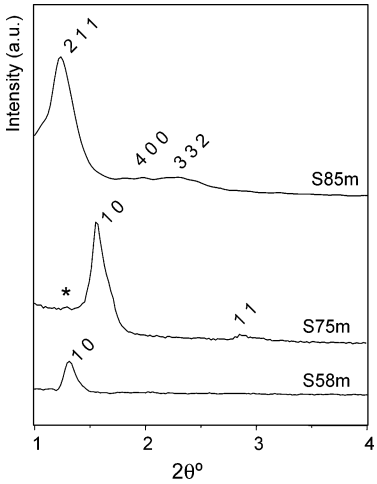

Figure 1. XRD patterns of the mesoporous $SiO_2-CaO-P_2O_5$ glasses prepared using $EO_{20}PO_{70}EO_{20}$ triblock copolymer as the structure-directing agent through the EISA method.

size 23.5 mm × 23.5 mm) at 30 000× and 60 000× magnification using a low-dose condition. Fourier transform (FT) patterns have been conducted using a digital micrograph (Gatan). EDX analyses were performed with an Oxford model ISIS.

Assessment of in Vitro Bioactivity. Assessment of in vitro bioactivity was carried out on disk-shaped samples. For this purpose, 200 mg of powder was softly pressed as a disk of 12 mm in diameter. The disks were mounted vertically by means of platinum scaffolds and soaked in 40 mL of filtered simulated body fluid (SBF), in polyethylene containers at 37 °C under sterile conditions. SBF has a composition and ionic concentrations similar to those of human plasma.[49] Concentrations of Ca as well as pH levels of the solutions after soaking the disks of glass were determined using an Ilyte Na^+ K^+ Ca^{2+} pH system. Scanning electron microscopy (SEM) and Fourier transform infrared (FTIR) spectroscopy were used to study the evolution of the surface of the glass. SEM analyses were made on a JEOL 6400 microscope. FTIR analyses of the glass surfaces were carried out in a Nicolet Magma IR 550 spectrometer.

Results

Figure 1 collects the small-angle XRD patterns of the three mesoporous glasses after calcination. S58m glass shows a unique low intense maximum at $2\theta = 1.28°$. In principle, this pattern is consistent with a hexagonal structure with 1d pore channels oriented parallel.[50] This point was later confirmed by TEM studies. S75m glass shows two well-resolved maxima at $2\theta = 1.54°$ and 2.86°, corresponding to 10 and 11 reflections of a 2D-hexagonal phase with plane group *p*6*mm*. In addition, a very weak maximum can be distinguished at $2\theta = 1.27°$, corresponding to a secondary phase. Further TEM studies demonstrated that this maximum corresponds to the 11 reflection of a 2D-orthorhombic phase with plane group *p*2*mm*. Finally, S85m glass shows three diffraction maxima at $2\theta = 1.20°$, 1.99°, and 2.31°. When combined with TEM analysis (see below), these maxima can be indexed to the 211, 400, and 332 reflections of a 3D-cubic phase with space group $Ia\bar{3}d$. Table 2 collects the structural parameters calculated from the XRD patterns.

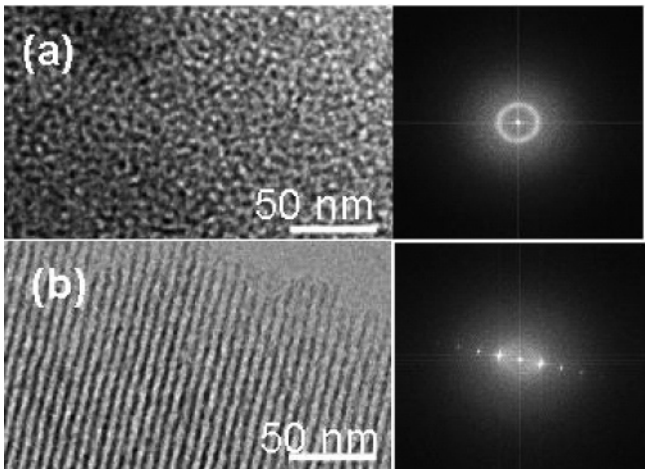

Figure 2. TEM images (left) and Fourier transform patterns (right) of calcined S58m obtained from different domains: (a) domain with poorly ordered wormlike structure referred to as "domain type 1" in the text and (b) hexagonal mesophase with 1d pore channels referred to as "domain type 2" in the text.

Table 2. Indexed Reflections for the Observed Peaks and Structural Parameters from the XRD Pattern

sample code	2θ	d_{hkl}/Å	*hkl*	a_0/Å
S58m	1.28	68.62	10 (*p*6*mm*)	79.24
S75m	1.27	69.47	11 (*p*2*mm*)	
	1.54	57.25	10 (*p*6*mm*)	66.16
	2.86	30.86	11 (*p*6*mm*)	
S85m	1.20	73.58	211 ($Ia\bar{3}d$)	180.23
	1.99	44.24	400 ($Ia\bar{3}d$)	
	2.31	38.23	332 ($Ia\bar{3}d$)	

Table 3. Indexed Reflections for the Observed Peaks and Structural Parameters from the FT Patterns

sample code	structure	d_{hkl}/Å	*hkl*	a_0/Å
S58m	2D-hexagonal (*p*6*mm*)	66.62	10	76.92
S75m	2D-hexagonal (*p*6*mm*)	66.31	10	76.57
		38.51	11	
	2D-orthorhombic (*p*2*mm*)	57.26	20	$a = 114.67$ $b = 80.26$
		40.13	02	
		65.75	11	
S85m	3D-cubic ($Ia\bar{3}d$)	70.142	112	171.81
	[110]	64.924	220	
	[110]	40.780	004	
	[110]	36.971	332	
	[111]	70.03	112	
	[111]	57.87	220	

HRTEM images for S58m mesoporous glass show that this material is composed by two different domains. The first domain (Figure 2a) shows a mesostructure composed exclusively of poorly ordered wormlike aggregates. The second domain exhibits channels with 2D-hexagonal symmetry (*p*6*mm*) with the interplanar space calculated as 76.92 Å, in good agreement with that determined by XRD (79.24 Å).

(49) Kokubo, T.; Kushitani, H.; Sakk, S.; Kitsugi, T.; Yamamuro, T. *J. Biomed. Mater. Res.* **1990**, *24*, 721.
(50) Lu, Y. F.; Ganguli, R.; Drewien, C. A.; Anderson, M. T.; Brinker, C. J.; Gong, W. L.; Guo, Y. X.; Soyez, H.; Dunn, B.; Huang, M. H.; Zink, J. I. *Nature* **1997**, *389*, 364.

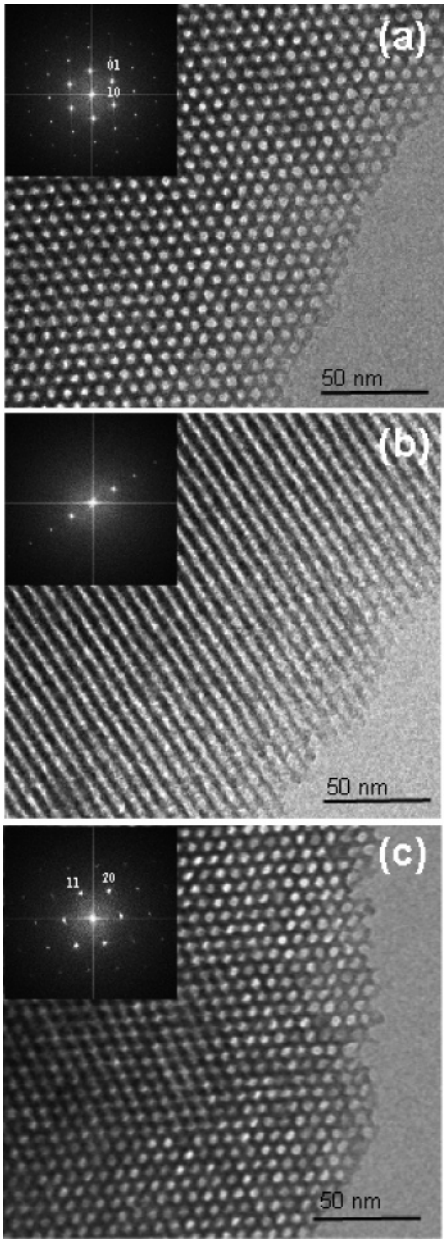

Figure 3. TEM images and Fourier transform patterns of calcined S75m obtained from different domains: 2D-hexagonal S75m recorded (a) along the direction parallel to the channels and (b) along the direction perpendicular to the channels; (c) 2D-orthorhombic S75m recorded along the direction parallel to the channels.

The structural parameters calculated from HRTEM are collected in Table 3.

HRTEM images and their corresponding FT diagrams of S75m glasses are shown in Figure 3. This sample shows two different highly ordered mesostructured phases. The main phase (Figure 3, parts a and b) corresponds to a 2D-hexagonal symmetry with a *p*6*mm* plane group. Figure 3c shows the HRTEM image and the FT pattern for the minor mesostructured phase of S75m. The HRTEM analysis demonstrates that this second domain corresponds to an orthorhombic structure with a plane group *p*2*mm* (see Table 3). Poorly ordered wormlike aggregates were not found in this sample.

Figure 4 shows HRTEM images and FT patterns of calcined Si85m taken with an incidence beam parallel to the

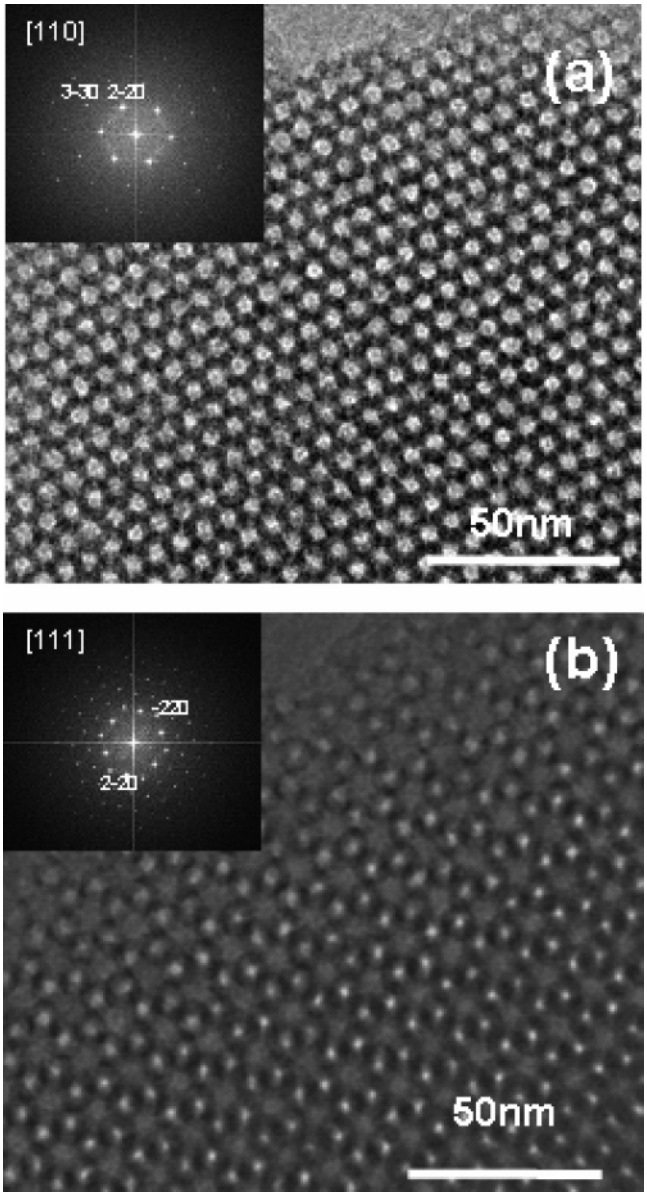

Figure 4. TEM images and Fourier transform patterns of calcined S85m: 3D-cubic S85m recorded along the (a) [110] and (b) [111] directions.

Table 4. Chemical Composition of the Mesoporous Glasses[a]

sample	Si	P	Ca
S58m nonordered	57.2	5.0	37.8
S58m *p*6*mm*	60.1	5.4	34.4
S75m *p*6*mm*	70.3	5.0	24.7
S75m *p*2*mm*	68.7	5.3	26.0
S85m $Ia\bar{3}d$	85.1	4.3	10.6

[a] Results of EDX analysis carried out on the different domains are collected.

[110] and [111] directions. The FT patterns clearly show the conditions for observable reflections: hkl, $h + k + l = 2n$; $0kl$, k and $l = 2n$; hhl, $2h + l = 4n$; $h00 = 4n$. From these observations, the space group symmetry was uniquely determined to be $Ia\bar{3}d$.

EDX analyses show the presence of silicon, calcium, and phosphorus homogeneously distributed into the different domains of the three samples (see Table 4).

Figure 5a shows the N_2 adsorption isotherms for the three mesoporous bioactive glasses (MBG) studied. All the curves can be identified as type IV isotherms characteristic of porous

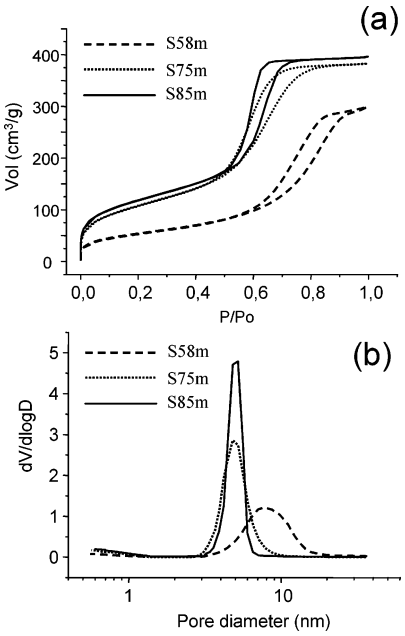

Figure 5. Nitrogen adsorption−desorption isotherm plots (a) and pore size distribution curves (b) of calcined mesoporous $SiO_2-CaO-P_2O_5$ glasses.

Table 5. Textural Parameters Obtained by N_2 Adsorption Porosimetry for Ordered Mesoporous Glasses[a]

	S_{BET} ($m^2 \cdot g^{-1}$)	ave pore diameter (nm)	pore vol ($cm^3 \cdot g^{-1}$)
S58m	195 (95)	9.45	0.46 (0.35)
S75m	393 (175)	6.0	0.59 (0.21)
S85m	427 (227)	5.73	0.61 (0.24)

[a] Values in parentheses correspond to textural values obtained for conventional sol−gel glasses with analogous compositions (refs 18, 47, and 51).

materials. The three samples show type H1 hysteresis loops in the mesopore range, which are characteristic of cylindrical pores open at both ends. The pore size distributions are shown in Figure 5b. All the samples present a single-modal pore size distribution centered around 6 nm for S75m and S85m, whereas S58m shows larger pores of about 9 nm.

Table 5 collects the S_{BET}, mesopore volume, and pore size measured for the three samples, which range between 99 and 227 $m^2 \cdot g^{-1}$ depending on the SiO_2 content. S_{BET} values are significantly higher than those obtained for conventional sol−gel glasses of analogous compositions. In the same way, pore volume is also higher for "ordered mesoporous glasses" compared to that of "conventional sol−gel glasses".

In Vitro Bioactivity Tests. Figure 6 shows the Ca^{2+} and pH values of SBF for different soaking time of glasses. Calcium levels increase for all the samples during the first 24 h after soaking the glasses. Thereafter, the calcium concentration slowly decreases until the end of the assay. Figure 6b plots the pH evolution of SBF as a function of soaking time. The pH evolution follows a profile analogous to that of the Ca^{2+} content. These results indicate that a $Ca^{2+}-H^+$ exchange occurs between the glass and the SBF, being more evident for mesoporous glasses with more calcium content (S58m > S75m > S85m).

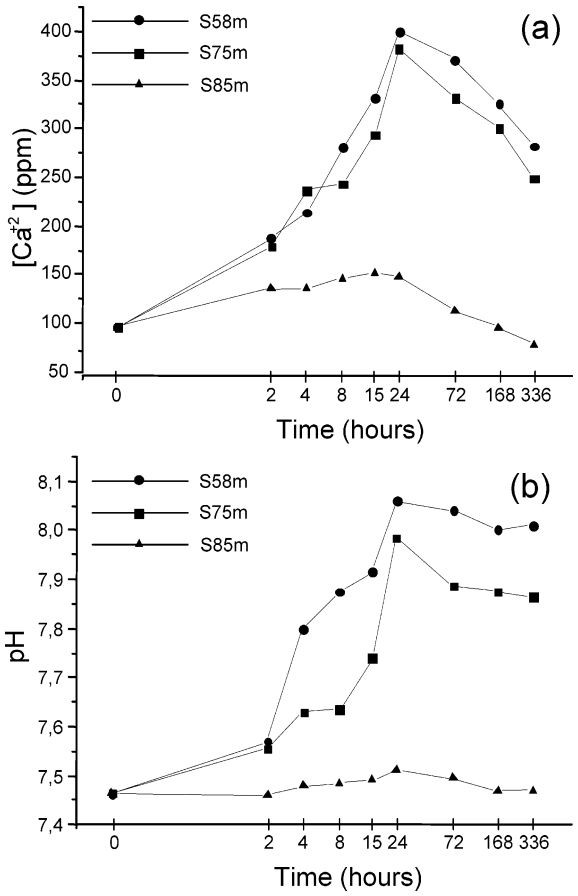

Figure 6. Variations of (a) calcium content and (b) pH values of the SBF after soaking the mesoporous $SiO_2-CaO-P_2O_5$ glasses.

FTIR spectroscopy was carried out to evaluate the changes in the glass surface as a function of soaking time. Figure 7 summarizes the most relevant spectra of each glass composition. Figure 7a collects the FTIR spectra of the S58m sample. Before soaking, the spectrum shows characteristic absorption bands of Si−O bonds at 1040, 800, and 470 cm^{-1}. After 2 h of soaking in SBF, an intense band at 600 cm^{-1} corresponding to an amorphous phosphate is observed. After 1 day of soaking, the band at 600 cm^{-1} begins to split into a doublet at 560 and 600 cm^{-1}, corresponding to a crystalline phosphate. The splitting becomes evident after 3 days in SBF, confirming the formation of a crystalline phosphate.

Figure 7b collects the FTIR spectra of the S75m sample. A similar evolution to that appreciated in S58m can be observed. An increase of the amorphous phosphate absorption band is observed after 2 h of soaking. An incipient PO_4^{3-} crystallization occurs after 8 h of soaking in SBF, being evident after 1 day of soaking.

Figure 7c shows the glass surface evolution of the S85m sample after different soaking times in SBF. A slight increase in the band corresponding to amorphous phosphate can be seen after 2 h of assay. The low intensity of this band indicates that a lower amount the newly formed CaP is deposited on the surface of S85m compared with that of the other mesoporous glasses. Nevertheless, crystallization of the new layer occurs after 4 h of soaking in SBF, i.e., faster than in the Si58m and Si75m samples.

Figure 8 shows the SEM micrographs of the mesoporous glasses after soaking in SBF. The micrographs reveal that

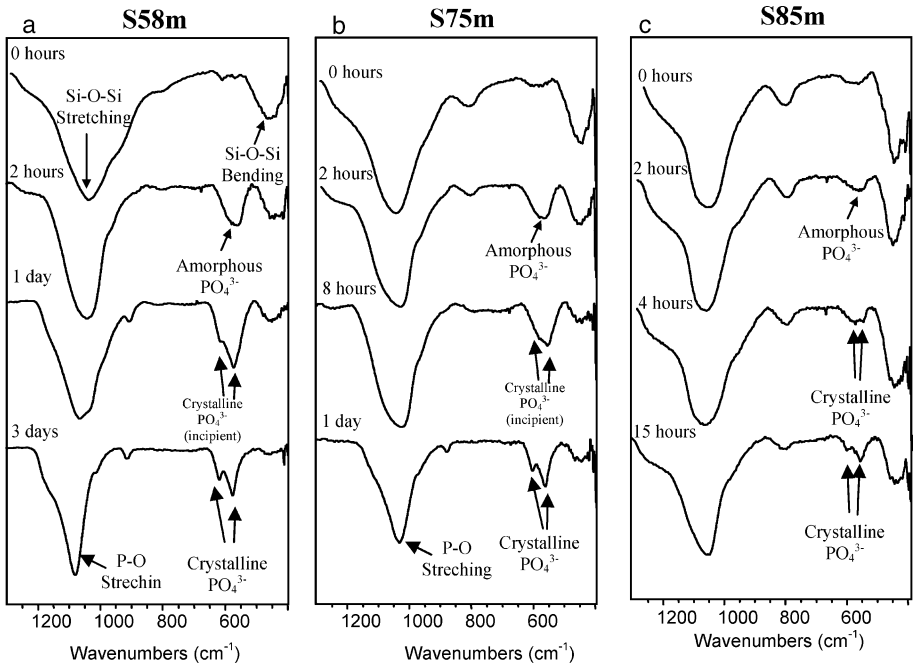

Figure 7. FTIR spectra for the different mesoporous $SiO_2-CaO-P_2O_5$ glasses as a function of soaking time.

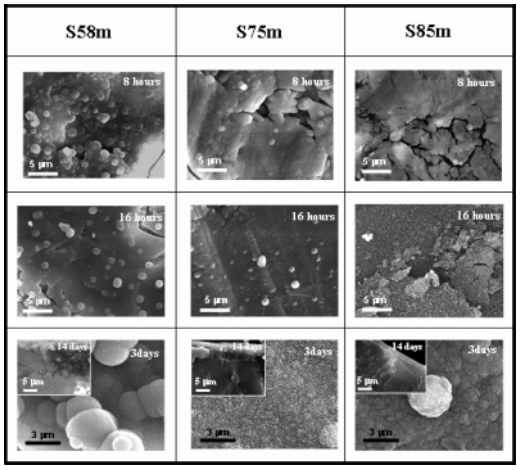

Figure 8. SEM micrographs obtained from the mesoporous $SiO_2-CaO-P_2O_5$ glass surfaces at different soaking times. The insets show a transversal section of the glasses after 14 days in SBF. The thickness of the new apatite layer grown on the surface can be easily observed.

the surface of the glasses undergoes important changes when reacting with SBF. After 8 h, S58m glasses are fully covered by a new phase composed of smooth spherical particles of around 1−2 μm in diameter. EDX analysis confirmed that the chemical composition of this new phase can be assigned to a Ca-deficient apatite phase (Ca/P ratio < 1.66). After 16 h the layer becomes thicker, whereas the rounded particles keep their smooth surface aspect. After 3 days of immersion in SBF, the surface of the glass is fully covered by larger rounded particles (around 3 μm or more). At the surface of these particles, some small needlelike crystals can be hardly observed.

The surface of the S75m sample undergoes a similar process as S58m after 8 and 16 h in contact with SBF. During the first 8−16 h of testing, the surface is fully covered by a layer composed of smooth rounded particles. After 3 days of assay, the needlelike shape of the crystallites can be distinguished covering the glass surface.

The morphological evolution of the surface in S85m mesoporous glass is different compared with that observed in S58m and S75m glasses. No morphological changes can be observed at the surface of S85m glasses after 8 h in SBF. This result is in agreement with FTIR experiments. After 16 h, a thin layer composed of needle-shaped crystallites is observed. Although this layer is significantly thinner than those grown on S58m and S75m for the same time, the evolution of the crystallites toward needle-shaped morphology is faster. After 3 days, an apatite layer of 2−3 μm thickness can be observed at the surface of this sample.

Discussion

The results obtained by XRD and TEM demonstrate that the structure of MBG depends on the added $Ca(NO_3)_2 \cdot 4H_2O$ amount. A progressive evolution from 2D-hexagonal to cubic structures is observed when decreasing the $Ca(NO_3)_2 \cdot 4H_2O$ content.

During the EISA process, preferential evaporation of ethanol (used initially to solubilize the organic precursors and homogenize the solution) progressively enriches the concentrations of water, HCl, and the nonvolatile solution constituents. Since the amounts of network former precursors (TEOS and TEP) and the amounts of structure-directing agent (P123) are the same for the three compositions, the structural differences must be understood as being a consequence of the different amounts of Ca^{2+} and water added as $Ca(NO_3)_2 \cdot 4H_2O$.

Therefore, two different mechanisms could lead to this structural evolution:

(1) Since the TEOS + TEP/P123 ratio is constant for all the glasses, the different amount of Ca^{2+} cations plays a very important role in the silica condensation. Ca^{2+} cations act as network modifiers, decreasing the network connectivity. Consequently, the inorganic/organic volume ratio is increased with the Ca^{2+} content, thus inducing the formation of hexagonal phases rather than cubic ones.

(2) The Ca^{2+} precursor, i.e., $Ca(NO_3)_2 \cdot 4H_2O$, supplies additional water molecules after dissolution. After ethanol evaporation, when the micellar concentration c_o > cmc (critical micellar concentration), c_o is lower for those compositions with more H_2O molecules released from the $Ca(NO_3)_2 \cdot 4H_2O$ (see Table 1). Since lower c_o's induce the formation of hexagonal phases rather than cubic ones, this mechanism would also be in agreement with the experimental results.

At the drying stage, i.e., before surfactant calcination, the materials possess membrane morphology of several hundred micrometers in thickness, as a consequence of the evaporation process in a Petri dish. During the formation of these membranes, the different silica−surfactant micelles concentration of each sample leads to different mesophases (by mesophase, we refer to the phase of the liquid-crystalline compound between the crystalline and the isotropic liquid phase). The coexistence of a 2D-hexagonal ordered phase together with a nonordered wormlike structure in S58m can be explained by the mechanism proposed by Lu et al.[50] for mesoporous thin films formation. After ethanol evaporation, the c_o exceeds the cmc value. Beyond the cmc, incipient liquid-crystalline domains grow from both substrate (Petri dish)−liquid and liquid−vapor interfaces toward the center by coassembly of silica−surfactant micellar species. Solidification at the drying establishes a structure composed of disordered cylindrical micelles (domain type 1, see Figure 2a) sandwiched between ordered regions of hexagonal mesophases (domain type 2, see Figure 2b). For samples with lower $Ca(NO_3)_2 \cdot 4H_2O$ content, i.e., higher c_o and lower Ca^{2+} content, the mesostructures evolve to a well-defined 2D-hexagonal structure together with a minor orthorhombic phase (sample S75m) or cubic phase (sample S85m) in response to the silica−surfactant micelles enrichment.

The textural studies demonstrate that "ordered mesoporous glasses" possess better textural properties compared to those of "conventional sol−gel glasses". Conventional $SiO_2-CaO-P_2O_5$ sol−gel glasses synthesized by our research group with identical or very similar composition showed S_{BET} values of 95, 198, and 227 $m^2 \cdot g^{-1}$ for S58, S75, and S85 compositions, respectively. When surfactant P123 is incorporated, the S_{BET} values increase until 195, 393, and 427 $m^2 \cdot g^{-1}$ for S58m, S75m, and S85m, respectively (see Table 5). The surfactant addition increases the S_{BET} value around 200 $m^2 \cdot g^{-1}$, with respect to the surface of "conventional sol−gel glasses", except for S58m, which only increases around 100 $m^2 \cdot g^{-1}$ when P123 is added.

The pore volume is also increased compared with that of "conventional sol−gel glasses", but S58m shows lower values than S75m and S85m. These data could be understood as contradictory, since it is well-known that Ca^{2+} incorporation leads to an increase of the pore volume in conventional sol−gel glasses.[51] However, in "ordered mesoporous sol−gel glasses", the textural features are ruled by the porosity coming from the surfactant calcination, as was previously demonstrated by Yan et al.[14] As an assumption, we can consider that not all the surfactant acts as an effective structure-directing agent in S58m, and therefore the textural properties do not increase as much as they do in S75m and S85m. These results are in agreement with the lower ordering observed by XRD and TEM for S58m and point out that the high Ca^{2+} content interferes with the surfactant, thus partially avoiding the structural mesophase formation when $c_o \geq$ cmc.

The "ordered mesoporous glasses" are highly bioactive, as indicated from the fast apatite-like phase formation when they react with SBF. The Ca^{2+} content and the pH evolution in SBF point out that an ionic exchange between Ca^{2+} from the glass and H^+ from the SBF takes place. In agreement with Hench's theory, this process leads to the silanol (Si−OH) formation on the glass surface. This step is mandatory for the subsequent apatite precipitation.

The FTIR results together with SEM observation confirm the bioactivity of these materials.

In "conventional" $SiO_2-CaO-P_2O_5$ sol−gel glasses, the main factors that contribute to the crystallization of an apatite phase on the surface are the CaO content and textural properties. A higher amount of CaO leads to lower network connectivity, thus improving the glass reactivity. The numerous works carried out on this system have shown that the CaO content is the main factor that provides bioactivity to the glasses.[18] The "ordered MBG" show this trend when considering the formation of an amorphous calcium phosphate (ACP) on the surface when soaked in SBF. The higher amount of Ca^{2+} cations released from S58m and S75m leads to the fast formation of a thicker ACP layer compared with that of S85m. The SBF becomes oversaturated, and ACP precipitates on the glass surface. Pereira[52] has indicated that Ca^{2+} concentrations higher than 200 ppm in SBF induce both homogeneous and heterogeneous CaP precipitation. Since both S58m and S75m reach a Ca^{2+} concentration of 400 ppm, we must consider that homogeneous precipitation of CaP highly contributes to the thickness of the CaP layer formed on these glasses. However, MBG show a different trend with respect to the apatite crystallization, in such a way that apatite crystallizes before on glasses with higher surface area but lower CaO content, i.e., S85m. Crystalline CaP is detected by FTIR after 4 h in S85m, whereas S58m and S75m show the first traces of crystalline CaP after 24 and 8 h, respectively. SEM observation follows the same trend. Characteristic needle-shaped crystallites of biomimetically grown apatite can be observed after 16 h in S85m and after 3 days in S58m (traces) and S75m.

The S85m sample shows a very interesting property as a material for bone filling and regeneration. One of the problems of bioactive sol−gel glasses is their "excessive" reactivity due to the initial burst effect of Ca^{2+} release. The intense ionic exchange during the first stages of the bioactive process leads to local pH increase. Depending on the sink conditions of the area (blood perfusion, mainly) the pH increase can be toxic for the surrounding tissues. S85m is a sol−gel glass that does not produce significant pH increase,

(51) Balas, F.; Arcos, D.; Pérez-Pariente, J.; Vallet-Regí, M. *J. Mater. Res.* **2001**, *16*, 1345.

(52) Pereira M. Bioactive Gel-Glasses: Processing and Reaction Mechanism. Ph.D. Dissertation, University of Florida, Gainesville, FL, 1994.

as the Ca^{2+} release is very low. However, S85m shows the best crystalline apatite rate formation due to its excellent textural properties and structural characteristics. This sample presents a 3D-cubic structure which exhibits a high diffusion transportation mechanism compared with that of 2D-hexagonal structures.

As a final comment, the potential application of these glasses as drug delivery systems or as osteogenic agent carriers should be noted. Studies in this field are currently in progress and will be the object of future publications.

Conclusions

Highly ordered mesoporous $SiO_2-CaO-P_2O_5$ bioactive glasses have been obtained by means of the EISA method, using a nonionic triblock copolymer as the structure-directing agent.

For a constant ratio between the network former precursors (TEOS and TEP) and the surfactant, the structural, textural, and bioactive properties of the mesoporous glasses change as a function of the CaO precursor content, i.e., $Ca(NO_3)_2 \cdot 4H_2O$.

The high surface area and porosity of these materials result in an excellent bioactive behavior. The textural parameters have more influence than chemical composition in the apatite crystallization stage of the bioactive process.

These materials are excellent candidates as grafts for bone tissue regeneration.

Acknowledgment. The financial supports of CICYT Spain, through Research Project MAT2005-01486, CAMS-0505/MAT/000324 VR: Sweden, and JST Japan (O.T.) are acknowledged. D.A. is grateful to MEC for the financial support through a "Ramón y Cajal" postdoctoral Grant. I.I.-B. is grateful to MEC for the financial support through a postdoctoral fellowship. We also thank to the Electron Microscopy Center, Universidad Complutense, and F. Conde (C.A.I. X-ray Diffraction, Universidad Complutense) for their valuable technical assistance.

CM060488O